EGTRIB Journal
JOURNAL OF
THE EGYPTIAN SOCIETY OF TRIBOLOGY
VOLUME 21, No. 4, October 2024, pp. 135 - 166 **ISSN 2090 - 5882**
(Received July 28. 2024, Accepted in final form August 29. 2024) **jest.journals.ekb.eg**

WEAR PREDICTION IN AXIAL PISTON PUMPS USING FINITE ELEMENT MODELING

Mohamed H. El-shazly[1], Shenouda A. Zaki[2]

Department of Mechanical Design and Production Engineering, Cairo University, Giza, EGYPT.

ABSTRACT

The service life of axial piston pumps, renowned for their high power-to-weight ratio and durability, can be compromised by wear, leading to safety risks and costly maintenance. This study investigates the factors that reduce service life, focusing on adhesive wear in the barrel-valve plate contact pair. A dynamic model based on the finite element method (FEM) is developed to predict wear using Archard's theory, while a computational fluid dynamics (CFD) model evaluates internal pressure distribution. The analysis shows that differential pressure causes the barrel to tilt toward the valve plate, accelerating wear. Through the design of experiments (DOE) techniques, the impact of critical operational parameters - discharge pressure and rotational speed - is quantified, revealing their significant influence on wear rates. Low pressure and speed increase wear, emphasizing careful management of these conditions. Additionally, load fluctuations accelerate wear, underscoring the importance of maintaining consistent operating conditions. Understanding these factors can help extend the service life of axial piston pumps, improve safety, and reduce maintenance costs.

KEYWORDS

Wear, axial piston pump, finite element method, computational fluid dynamic, ARCHARD theory

INTRODUCTION

The swashplate axial piston pump is a widely used positive displacement pump in hydraulic circuits for both mobile machinery and industrial applications. Its appeal lies in its high volumetric and mechanical efficiencies, reaching up to 95 %, and its ability to operate at pressures as high as 700 bar, [1, 2]. Its high-power density and small weight-to-power ratio make it particularly suitable for mobile and aviation applications. These pumps come in a range of flow capacities up to 1000 l/min and offer both variable and fixed displacement options for enhanced hydraulic system control, [3]. To meet strict environmental regulations and conserve energy, high-pressure, high-performance axial piston hydraulic pumps must be driven efficiently by a primary mover, such as a thermal or electric engine. Gordon Mohn et al., [4] Illustrated this by showing how increasing the nominal pressure of the A4VSO series

to 630 bar reduced the horsepower required to drive the pump. For aviation hydraulic systems, Shengrong Guo et al., [5] Emphasize that increased rotational speed and high pressure are necessary to enhance aircraft capability and maneuverability. Electro-hydrostatic actuators, which improve flight safety and precision, are also crucial. However, these requirements pose practical challenges for pumps, such as pressure pulsation and cavitation. One major issue is barrel tilt, which significantly reduces the pumps' service life and challenges the tribological design of contact surfaces.

In practical scenarios, unexpected axial piston pump failures often cause machinery downtime, leading to safety hazards and substantial expenses. Visual inspections of failed pumps frequently identify wear as the primary cause of breakdowns. However, the exact factors contributing to high wear rates remain unclear, especially when pumps fail prematurely, well before their expected lifespan of 20,000 hours, despite being well-maintained and operated under normal conditions. Therefore, this study aims to present a systematic approach to predicting wear in axial piston pumps, focusing on understanding and mitigating the factors that lead to reduced service life.

Swashplate axial piston pump design and working principle.

The swashplate axial piston pump, as shown in Fig. 1, consists of a cylinder block (barrel) with several cylindrical cavities evenly spaced around its circumference. Typically, these pumps have an odd number of cavities, with seven or nine being the most common configurations. A piston or plunger is housed inside each cavity, which is forced to reciprocate. The piston features a spherical end supported by a piston shoe, also known as a slipper. This slipper rests on the swashplate, forming a spherical bearing with the piston's spherical end. The swashplate is an inclined plate fixed to the pump housing at an angle relative to the pump's lateral axis. This inclination controls the stroke of the pistons and, consequently, the pump's output flow. By adjusting the angle of the swashplate, the pump's displacement and output volume can be varied.

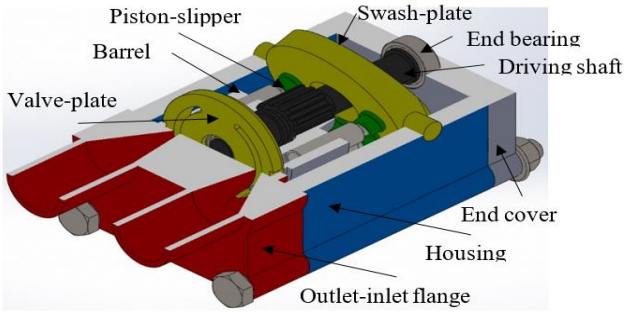

Fig. 1 Simplified drawing for the main component for the Swashplate axial piston pump.

The circular valve plate remains stationary and features two kidney-shaped openings that function as suction and discharge ports. The barrel and valve plate are in contact with the valve plate connected to the outlet/inlet flange. A compression spring presses the barrel against the valve plate, controlling the clearance between them. The stiffness of this spring is a critical design parameter for maintaining the proper gap and ensuring effective operation. The pump internal components must be ma nufactured with extremely tight tolerances and a high-quality surface finish. These components are typically made from high-strength materials to withstand the high operating pressures and ensure effective sealing. In most designs, sealing is achieved through precise clearances, with no additional sealing elements. Numerous sliding surfaces within the pump generate friction and are subject to wear. The most critical tribological pairs, which significantly influence pump performance and service life, are illustrated in Fig. 2. These include the barrel-valve plate, piston-cylinder bore, and swashplate-slipper interfaces.

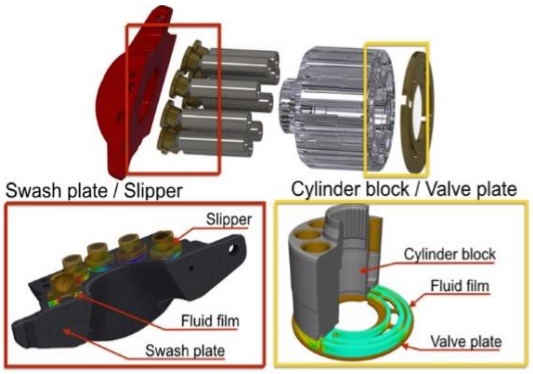

Fig. 2 Summarizing of Tribological pairs, [6].

The lubricant film in an axial piston pump has two primary functions: sealing and supporting the mating surfaces. The clearance typically ranges from ten to twenty microns or less in a well-conditioned pump, [7]. Therefore, the dynamics of the movable components and the lubrication characteristics are critical factors in predicting wear and friction within the pump. Each tribological pair exhibits different behaviors under load, influencing the pump overall performance and service life. This study focuses on the barrel-valve plate pair, which is the major contact area and experiences the highest wear rates.

Due to the pressure differential between the suction and discharge sides, the barrel is subjected to a tilting moment. This affects the height of the lubricant film between the cylinder block and the valve plate, potentially leading to metal contact. The first step is to analyze the dynamics of the cylinder block to better understand wear rates and lubrication film behavior. In two papers, A.Yamguchi, [8, 9], calculated the forces acting on the cylinder block. The first paper demonstrated that even small changes in loading conditions significantly affect the height of the lubrication film between the barrel and the valve plate. Their second paper proposed adding a pad to the valve plate's sealing surfaces to improve the bearing capacity and stabilize the lubrication film. Similarly, David Richardson et al., [10, 11]. They conducted experimental

studies on floating valve plate motion under varying loads. Their lubrication model revealed that minimum film thickness decreases as discharge pressure increases, leading to more significant spikes and drops in lubrication pressure. Interestingly, they found that rotational speed had little to no effect on the film thickness, suggesting that hydrostatic lubrication mechanisms dominate the barrel-valve plate gap. Moreover, a review of advanced lubrication models, [12]. It confirmed that hydrodynamic lubrication is crucial in barrel tilting, with both discharge pressure and rotational speed as critical factors. Fredrik Roseline, [13], mentioned a similar conclusion, applying the "Lulea Mixed Lubrication" (LMLM) model to analyze the tribological surface behavior in a PARKER hydraulic machine. Fig. 3 illustrates the effect of barrel tilting on the shape of the lubrication layer, where a wedge-shaped film is formed, amplifying the hydrodynamic effect.

Once the barrel's dynamic behavior and lubrication characteristics have been established, wear prediction becomes feasible. G. Schuhler et al. experimentally studied the wear mechanism in worn pumps, [14]. The study identified the primary wear mechanism as three-body abrasive wear caused by carbides in the slipper lands due to oil contamination. Additionally, it revealed that two-body abrasive wear occurred when the lubrication film failed. Abrasive wear in axial piston pumps was further investigated by C. Zhan et al., [15], who developed a mathematical model based on the Reynolds equation and Hertz's abrasion theory. This model analyzes the wear progression on tribological surfaces due to abrasive forces. In combination with online wear debris analysis, Zhan's model was used to track performance degradation and estimate wear volume, providing a correlation between working conditions and the progression of surface seizure. Furthermore, Daniel Nilsson, [16]. The seizure progression of sliding surfaces was evaluated numerically, linking wear rates to operational conditions. The following section explains a methodology to simulate the pump dynamic.

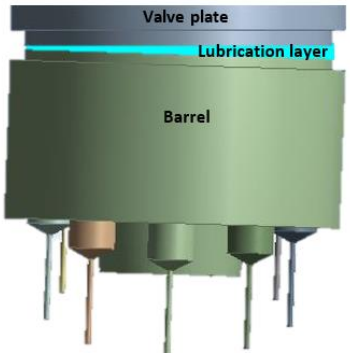

Fig. 3 Barrel tilting explanation and the lubrication layer shape.

Swash Plate Axial Piston Pump Modelling

Creating the geometrical model is the first step in modeling a system using Finite Element Analysis (FEA) or Computational Fluid Dynamics (CFD). This is accomplished using a CAD software package. The following sections describe the selected axial piston pump's geometric, fluid, and dynamic models.

Geometric model

This analysis uses the EATON VICKERS PVB5 swashplate axial piston pump as the case study. Li has studied its flow characteristics, [17], allowing for model validation. The CAD model of the pump was created using the SolidWorks 2018 software package, as shown in Fig. 4 - a, while the dimensions and specifications of the pump assembly are detailed in Fig. 4 - b.

Computational Fluid Dynamic (CFD) Model

For simplicity, the housing, bearings, and control valves have been excluded from the model. The CAD software cavity extraction tool was used to extract the fluid volume. As shown in Fig. 5. The volume is divided into stationary zones that contain discharge, suction, valve plate passages, and barrel outlet slots, whose mesh size does not change over time, and dynamic zones, which contain fluid inside the barrel cavities, including clearances between pistons and cylinders that mesh dynamically changes with time by dynamic mesh layering technique, in addition to the piston's internal volumes, which move as rigid bodies. The gap between the barrel and valve plate is filled by a ring shape that simulates the lubrication layer and is considered stationary. The CAD file was then transferred to the CFD solver to discretize and build a model.

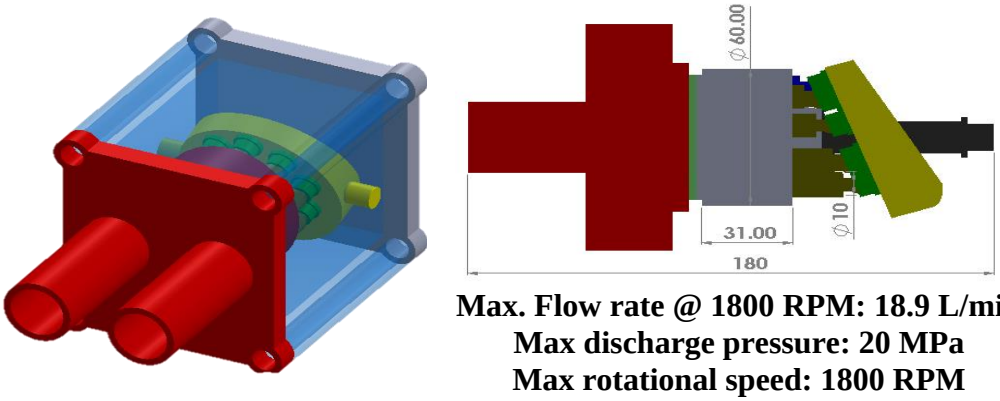

Max. Flow rate @ 1800 RPM: 18.9 L/min
Max discharge pressure: 20 MPa
Max rotational speed: 1800 RPM

(a) **(b)**

Fig. 4 PVB5 Axial piston pump, (a) CAD drawing, (b) pump aspeces.

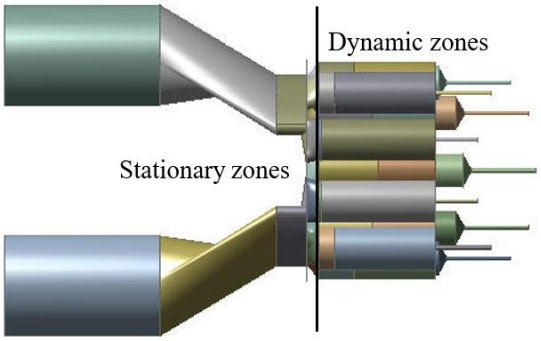

Fig. 5 Internal fluid volumes as extracted from CAD drawing.

To successfully simulate the pump flow, the interaction between zones must be considered. The suction and discharge zones at their interface surfaces interact with the lubrication layer between the barrel and valve plate. A sliding interface mesh type enables fluid exchange between the valve plate and the outlet zones through the lubrication layer. The piston crown and the clearance top are connected to the lower cylinder zone, so matching mesh interference is used, allowing fluid flow between zones.

Fluid Flow Modelling

The flow field inside an axial piston pump is highly non-linear and three-dimensional. To model this, the Reynolds-Averaged Navier-Stokes (RANS) equations and continuity equations in a Cartesian coordinate system are employed for compressible-turbulent flow, as detailed by B. Andersson et al., [18].
The following assumptions are made:

- **The flow is time-dependent, isothermal, and turbulent, while the flow inside clearances is considered laminar.**
- **The fluid is compressible, density-dependent solely on pressure, and molecular viscosity is constant.**
- **The pump is assumed to be cavitation-free, which is reasonable at low to medium angular velocities with positive suction pressure.**

The k-ε RNG turbulence model is implemented, which, with the RANS equations, allows for the estimation of the flow field variables within the pump.

Geometry discretization

The fluid cavities must be discretized using appropriate mesh elements to solve the flow equations. Mesher was used for this purpose, as shown in Fig. 6, which illustrates the discretized fluid zone model. Choosing mesh element type and density is crucial to balancing accuracy and computational cost. Therefore, a trade-off between element type, element count, and accuracy is necessary to select the optimum grid for the simulation. As shown in Fig. 7, the dynamic fluid zones are discretized using uniform grid elements (hexagonal elements), which can be swept in the flow direction to facilitate the layering dynamic mesh technique. The piston volumes move as rigid bodies. For the stationary zones, except for the pipes, mixed grid elements are used, significantly reducing the mesh size without compromising accuracy. To accurately assess the leakage and pressure distribution within the clearance, six mesh elements are placed in the radial direction across the lubrication layer, as shown in Fig. 8. However, the discharge and suction pipes are discretized with a uniform grid that becomes denser toward the valve plate zone. Due to their geometric complexity, the valve plate and curved sections are discretized using a mixed grid, with mesh refinement applied at transition grooves to enhance calculation accuracy.

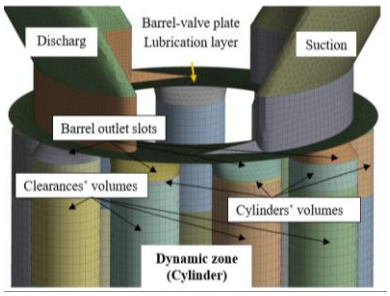

Fig. 6 CFD model discretized zones; uniform grid is used with dynamic mesh while tetrahedron elements discretize stationary zones.

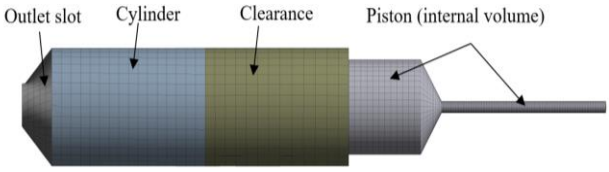

Fig. 7 Piston, Cylinder, and clearance internal volumes mesh.

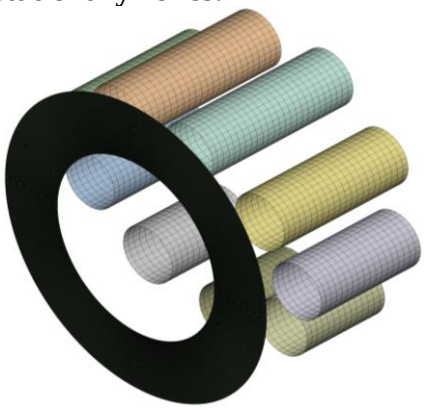

Fig. 8 Clearances fluid mesh.

1.1.1 Boundary Condition

A loaded hydraulic circuit resists the pump outlet port, while in pump testing, the pump's outlet is connected to a needle valve, as described, [17].The outlet vent boundary condition creates a variable hydraulic load for the pump outlet. According to the CFD solver manual, [19], the pressure drop through the vent boundary is calculated by:

$$\nabla p = C_L \frac{1}{2} \rho v^2 \qquad \textbf{(1)}$$

Where C_L is loss coefficient, ρ is fluid density, and v is flow velocity, and the needle valve flow equation:

$$q = C_v A_v \sqrt{2 \times \nabla p / \rho} \qquad \textbf{(2)}$$

Where C_v is the needle valve discharge coefficient, and A_v is the discharge area through the valve, the rearrangement equation. (2), the pressure drop through the valve can be evaluated from,

$$\nabla p = \frac{1}{2} \rho \frac{q^2}{C_d^2 A_d^2} \qquad \textbf{(3)}$$

By equating equations(3) and(1), the loss coefficient C_L, evaluated by:

$$C_L = \frac{A_v^2}{C_d^2 A_d^2} \qquad \textbf{(4)}$$

Where A_d is the outlet cross-sectional area, which is 4e-4 mm^2 for the current model, the valve opening (Av) is adjusted with the help of the equation to meet the

requirement of discharging (resistance) pressure, (4). After some trials, the loss coefficient, CL, for different operating conditions can be estimated. The various clearance zones are filled with a ring-like oil film, as shown in Fig. 25. The outer circumferential surfaces are vented to the tank, with a pressure outlet boundary condition applied, maintaining zero-gauge pressure. A similar boundary is applied to the inlet port.

Piston-slipper side

The slippers and swashplate are excluded from the simulation to simplify the model. However, their effects are incorporated using a velocity outlet boundary condition assigned to the end of the piston (slipper side). The velocity profile is derived from the slipper leakage equation, initially proposed by J.M. Bergada et al., [20], and applied to the boundary using a User-Defined Function (UDF).

Solution Method

The pressure-based solver is used to solve the RANS equations for the fluid domain, employing a segregated discretization scheme. The pressure-velocity coupling is handled using the SIMPLEC scheme, while the gradient discretization scheme is second-order. The time gradient discretization uses a first-order scheme, and the turbulent parameters are solved using a second-order discretization scheme.

Time step and convergency criteria

A time step of 1e-4 seconds provides a suitable resolution to capture the flow changes within a complete revolution accurately. The residuals for continuity, momentum, and turbulence parameters are monitored at each time step, and the convergency limit is set to 1e-5 to ensure an accurate solution.

Mesh independency test

For reliable model solutions, the results should not change significantly with varying element numbers, [21]. To test mesh independence, the outlet flow rate and pressure ripples were evaluated for different mesh designs, as illustrated in Fig. 9. The solution curve levels off at around 1.2 million elements, indicating that the results become independent of mesh size at this point. Therefore, this mesh size will be used for all subsequent cases. All validation cases were run at 1800 RPM and 5 MPa.

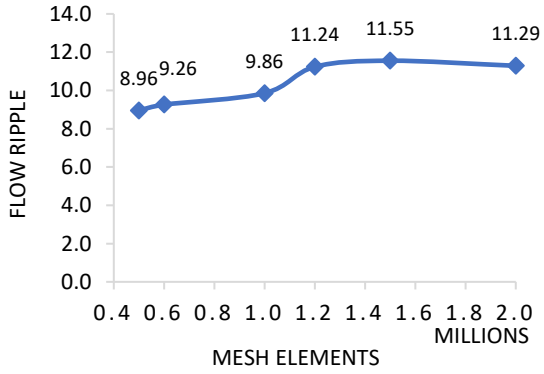

(a)

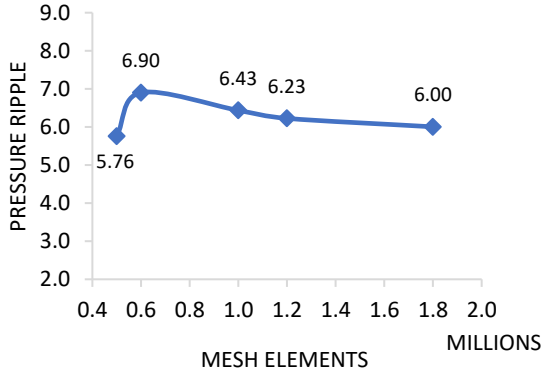

(b)

Fig. 9 Outlet ripples against element numbers (a) discharge pressure ripple and (b) outlet flowrate ripple.

Dynamic model

Introduction

After the pump components were modeled, the dynamic modeling of the axial piston pump was established using commercial finite element software. The material properties of the pump are listed in Table 1. To optimize computation, parts with negligible deformation are treated as rigid bodies.

Table 1 Material properties, [22].

Part	Material	Properties	
		E (GPa)	σ_y (MPa)
Barrel, Piston	Stainless Steel 316L	193	210
Valve plate, Slipper	Bronze	180	280
Swashplate, Shaft	Steel	200	250
material hardness $H = \sigma_y/3$, [23].			

Model Kinematic Joints

The primary goal of the current model is to determine the barrel's dynamic response under working loads, including its contact with the valve plate, pistons, and shaft. To address the contact interactions, the contact-target method is employed to solve the contact problem.

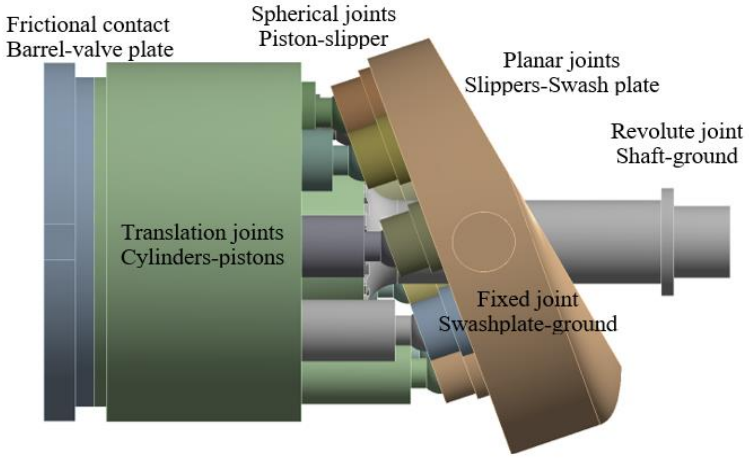

Fig. 10 Finite element model kinematic joints and non-linear contact.

The valve plate is fixed in all directions. A frictional contact with a coefficient of 0.02 has been established between the barrel and the valve plate, Fig. 10. The joint permits the barrel to move relative to the valve plate within a small clearance. The resulting contact pressure is evaluated if the barrel comes into contact with the valve plate. To maintain model efficiency, piston tilting is neglected, and a linear translation joint is

used between the cylinder and piston. So, piston inertia is considered, but friction is neglected.

The slipper, which supports the piston on the swashplate, is shown in Fig. 10. It is connected to the piston via a spherical joint that allows rotational movement of the piston relative to the slipper's axes without separation. The slipper is considered rigid for the model, with a density of 7856 kg/m^3. A frictional coefficient of 0.01 is applied, which is appropriate for the oil-lubricated joint. The swashplate is fixed to the ground through pinned ends and supported by the slipper, which slides over its surface. This allows the pistons to reciprocate inside the barrel cavities.

A planar joint with a friction coefficient of 0.01 is used. This joint allows the slipper to move over the surface of the swashplate without translation along the normal axis while permitting rotation around the normal axis. The barrel is connected to the shaft via splines. Due to the clearance fit, the barrel can tilt and translate axially along the splined shaft. A non-linear frictional contact is established between the barrel and the shaft, with a frictional coefficient of 0.1. The shaft is supported at both ends by rigid bearings, and a revolute joint is added between the shaft and the ground, allowing the shaft to rotate around its axis. The compression spring is modeled as a joint between the ground and the barrel, pushing the barrel toward the valve plate. A spring stiffness is 150 N/mm.

1.1.2 Model meshing

The process of converting the geometric model into a Finite Element Analysis (FEA) model is known as meshing. This process transforms lines, surfaces, and volumes into nodes with specific locations and connectivity. Due to the model's complexity, tetrahedral mesh elements are generally used. Additionally, local mesh sizing methods are applied to increase mesh density around the edges and faces of the contact zones, enhancing the accuracy of the model, as shown in Fig. 11.

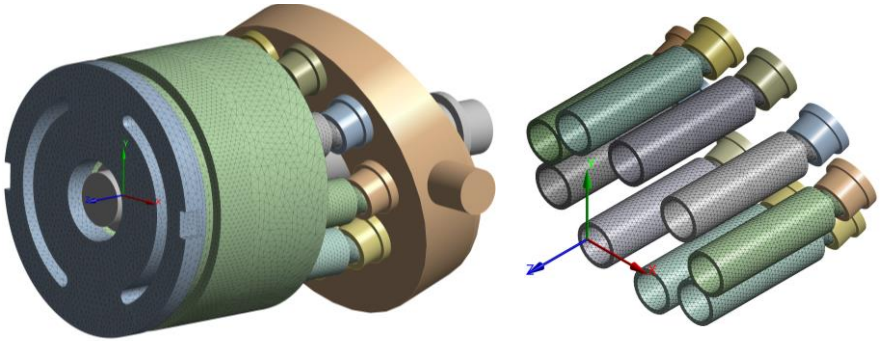

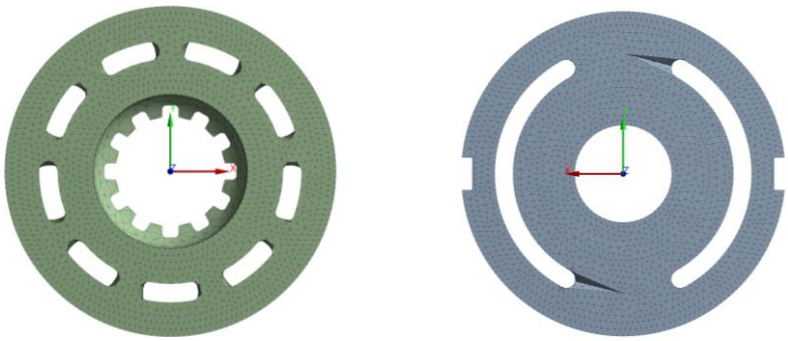

Fig. 11 Dynamic model mesh design.

Boundary conditions

The pressure forces exerted on the barrel must be included to complete the model. The surface pressure distribution is obtained from the CFD model and implemented using the external file connection feature. The pressure is then mapped over the corresponding surfaces of the barrel and piston walls. The shaft's angular displacement is also applied through the shaft revolution joint, ensuring one complete revolution is simulated in each run.

Wear calculation module

The adhesive wear volume was calculated based on Archard's model, [24],

$$Q = \frac{K \times W}{3H} \qquad \textbf{(5)}$$

Where Q is the wear volume per unit sliding distance (wear rate), the factor 1/3 is included in K for simplicity, [23, 25], where K is the non-dimensional proportionality wear factor, W is the normal load acting on the surface, and H is the material hardness or yield stress. According to the Archard model, as explained by J. Halling, [24], the wear rate is independent of the apparent area of contact and is instead proportional to the real area of contact, the normal load, and the material hardness. The dimensionality wear probability factor (*k*), [26]. This accounts for the fact that not all contact asperities experience wear. Its value typically depends on the material pair and load, ranging from 1×10−3 dry conditions to 1×10−6 lubricated conditions. The FE solver includes a built-in wear module based on Archard's theory, [19]. To enable the wear module, a special code must be written, and the material properties are implemented from Table 1, and the wear coefficient (K) is 1×10−6, [23]. The evaluated wear height over each iteration is stored and then averaged over the total number of iterations at the end of each solution case.

Mesh adaption

The accuracy of Finite Element Modeling (FEM) is closely tied to the number of mesh elements and the computational resources required. Therefore, a balance must be struck between accuracy and computational efficiency. An adaptive meshing method is employed, with barrel total deformation chosen as the critical parameter for the mesh independence study. The relationship between mesh element count and deformation is shown in Fig. 12, and the corresponding element numbers for each

solution iteration are provided in Table 2. As illustrated, barrel deformation decreases after the first adaptive iteration (solution number) and then begins to stabilize. After three iterations, the deformation variation reduces to less than 5 %. Therefore, solution number 3 is considered mesh-independent, and the corresponding mesh size is used for all subsequent simulations.

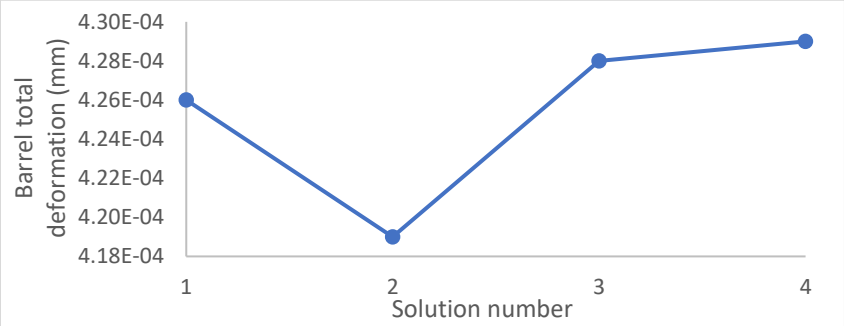

Fig. 12 Mesh adaptive curve as obtained from FE solver for the pump based on total deformation.

Table 2 Total deformation variation corresponding to element number.

Solution number	Total deformation (mm)	Elements number
1	4.26e-4	15505
2	4.19e-4	25486
3	4.28e-4	47349
4	4.29e-4	72771

Initial conditions Time step selection and Model solving method

The model assumes static balance at the start of the simulation, where the barrel is pressed against the valve plate by the spring's precompression force of 1500 N, before any pressure build-up occurs. The simulation runs with a fixed time step of 0.001 seconds, utilizing an auto-variable sub-step option to adjust as needed. The rotational speed determines the number of time steps, ensuring that one full revolution is completed within the total simulation time. The implicit Newton-Raphson method, with the full option enabled, [27], is used to solve the FEM model, with the large deformation feature activated to handle the complexities of the simulation.

ANOVA Study Preparation

The study's main objective is the influence of operating conditions on wear. The design of the experiment technique is implemented to select the optimum number of cases that should be performed; there are two factors (discharge pressure and rotating speed), and each one has four levels, so for full factorial design, fluid and dynamic models have to run sixteen number with different operating conditions, illustrated in Table 4

Table 3 Operating conditions performed in the study, based on the full factorial array.

Run number	Operating conations

	Pressure (MPa)	speed (RPM)
1	5	800
2	5	1200
3	5	1500
4	5	1800
5	10	800
6	10	1200
7	10	1500
8	10	1800
9	15	800
10	15	1200
11	15	1500
12	15	1800
13	20	800
14	20	1200
15	20	1500
16	20	1800

RESULTS AND DISCUSSIONS

CFD Model

Barrel Pressure Distribution

The primary objective of this study is to evaluate the pressure distribution on the barrel surfaces, as shown in Fig. 13. The pressure is assessed on the barrel's top, inner, and piston walls. The pressure distribution under different operating conditions is shown in Fig. 14 - Fig. 16. These figures indicate that while the overall pressure distribution pattern remains unaffected by the operating conditions, the pressure levels change according to the loss coefficient settings. These pressure distributions are then mapped onto the dynamic model's corresponding surfaces and operating conditions.

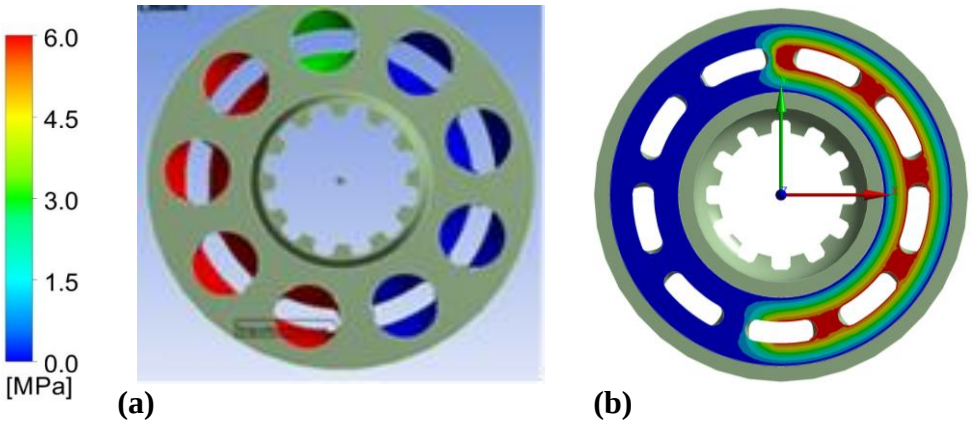

(a) **(b)**

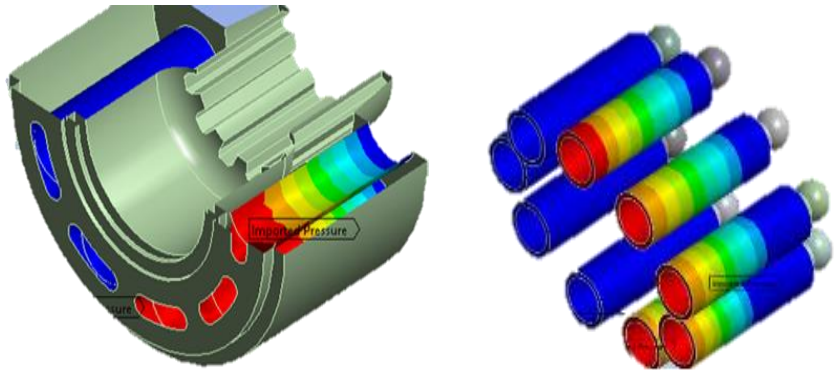

(c) **(d)**

Fig. 13 Pressure distribution over walls, (a) barrel inner surface, (b) barrel top surface, (c) barrel side walls and (d) piston walls.

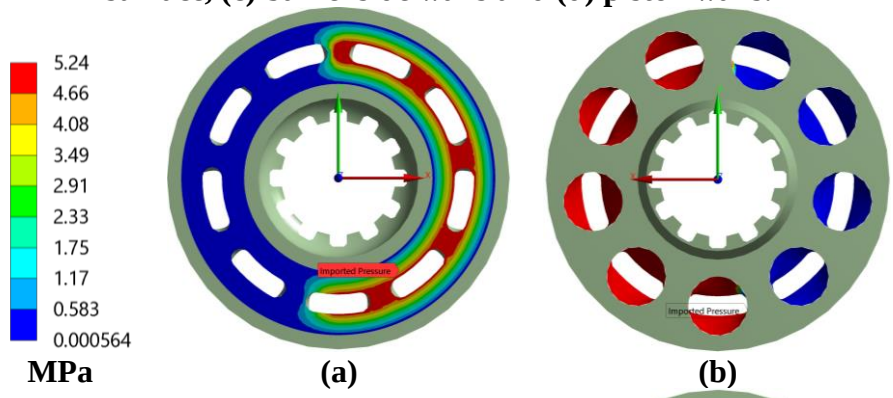

(a) **(b)**

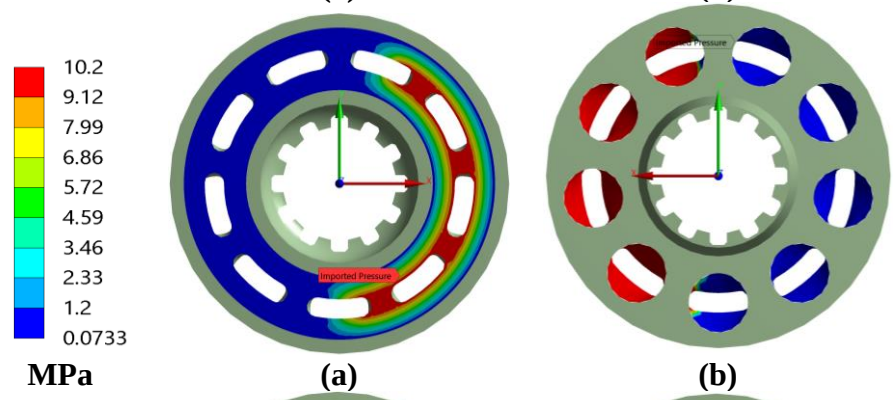

(a) **(b)**

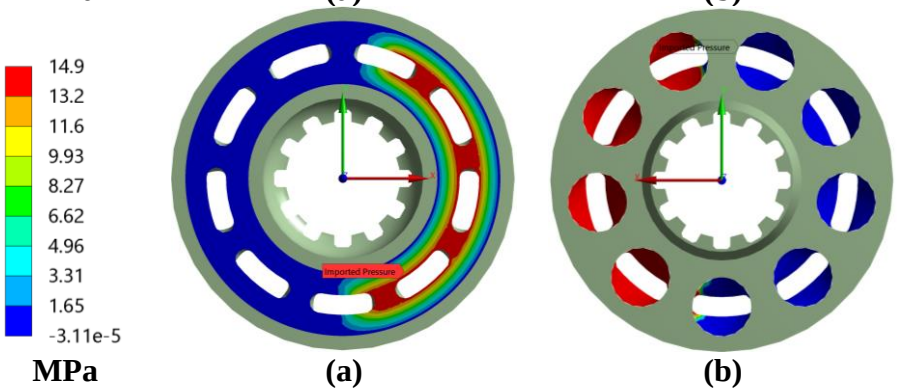

(a) **(b)**

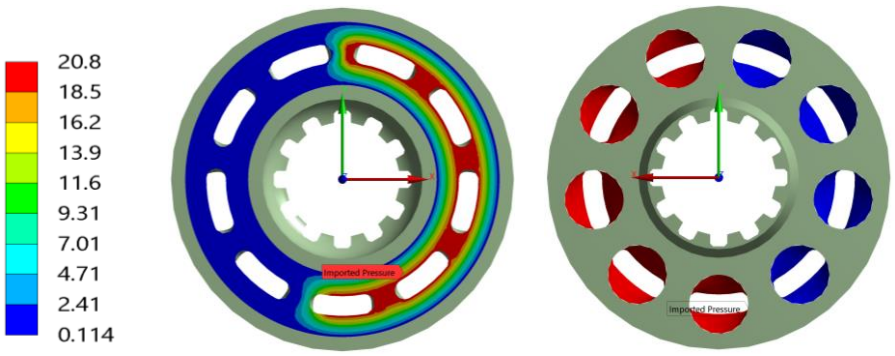

Fig. 14 Barrel pressure distribution for 800 RPM, (a) top surface, (b) internal surfaces.

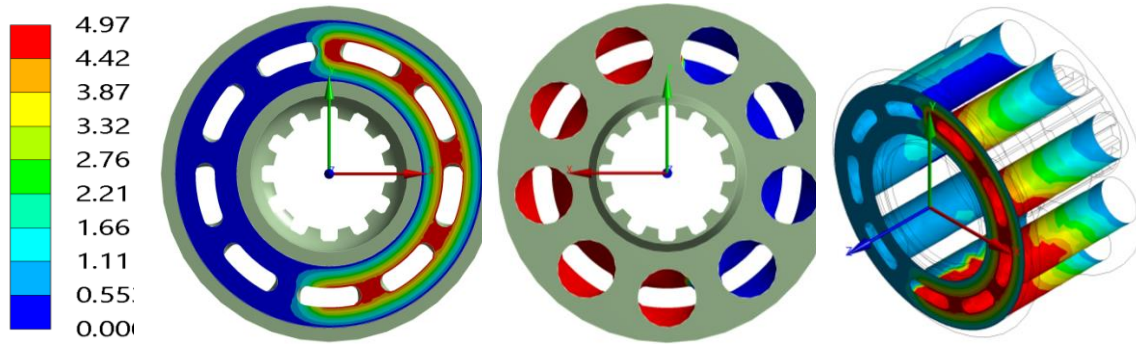

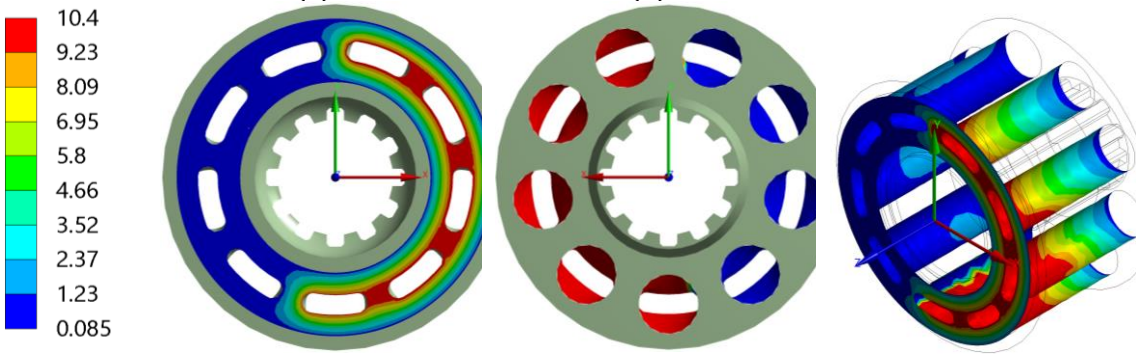

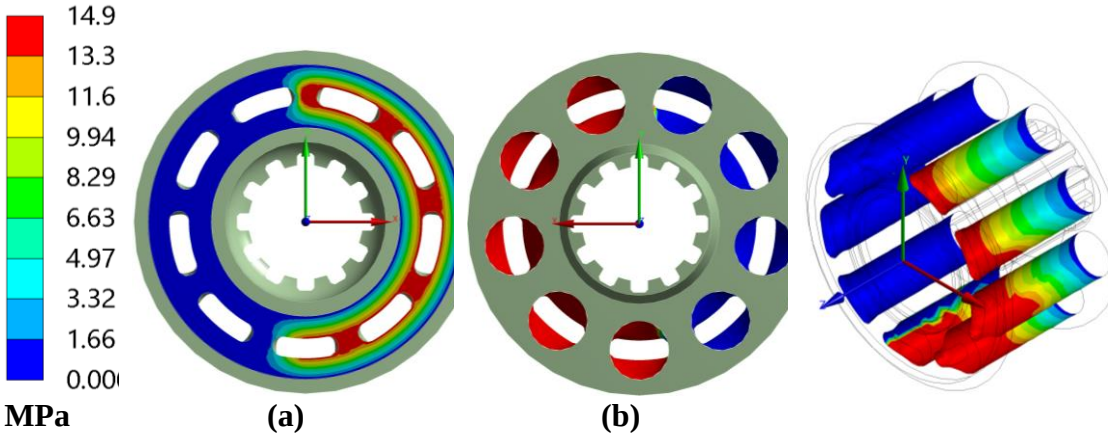

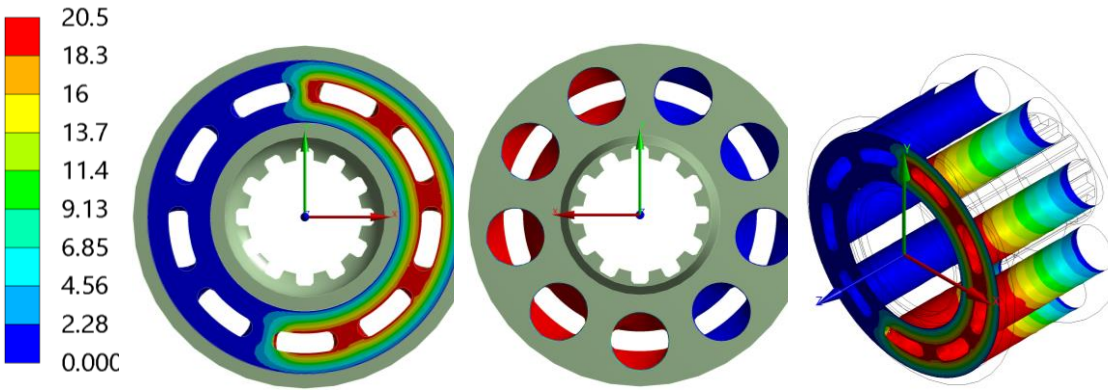

Fig. 15 Barrel pressure distribution for 1200 RPM, (a) top surface, (b) internal surfaces.

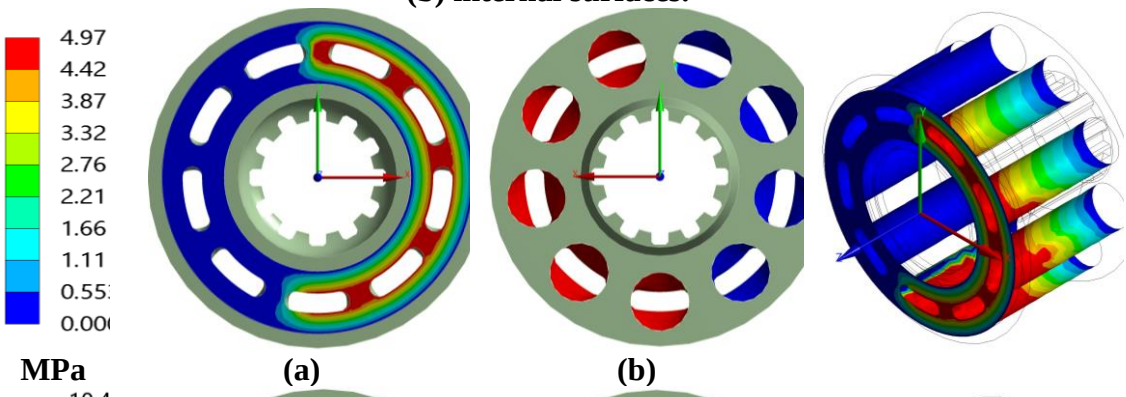

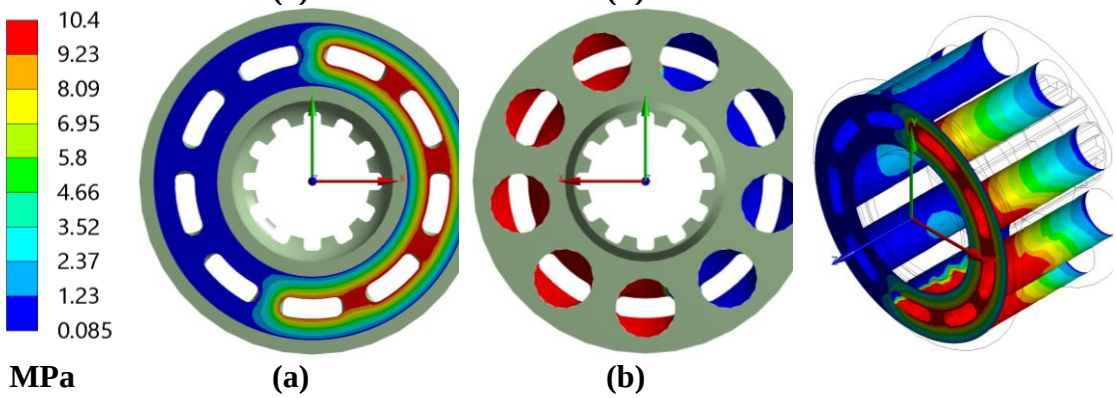

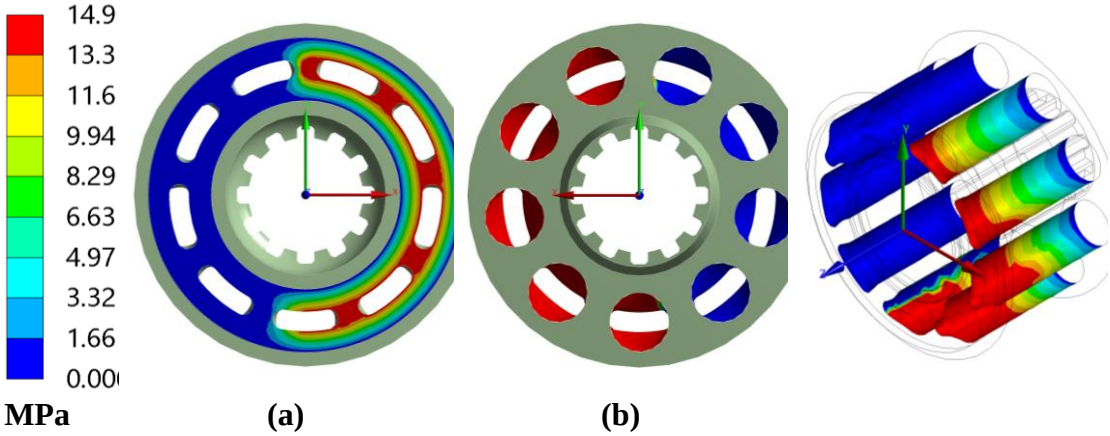

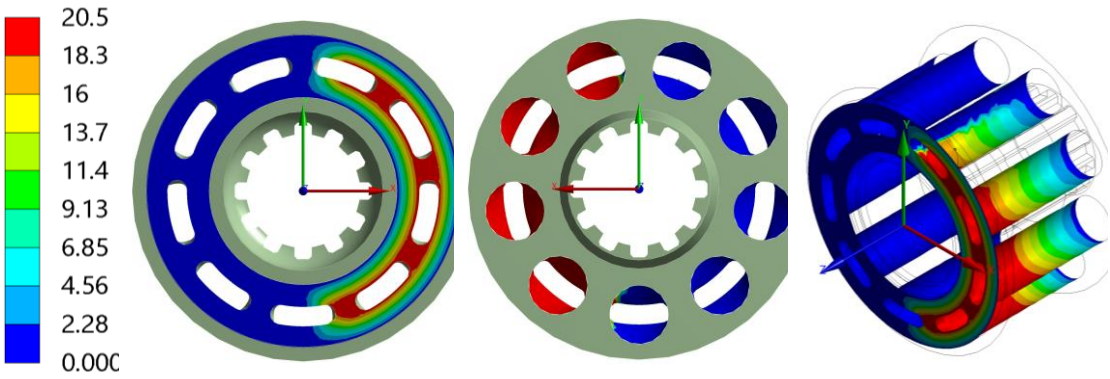

Fig. 16 Barrel pressure distribution for 1800 RPM, (a) top surface, (b) internal surfaces.

Ripple Flow Characteristics

The outlet flow ripples are shown in Fig. 17, and the pressure inside the barrel cavity changes with angular position, fluctuating between discharge and suction pressure levels, with over- and undershoots occurring at the transition zones. The piston pressure ripple is illustrated in Fig. 18-a. Pressure overshoots and undershoots occur due to flow transitions. As showing Fig. 18-b, pressure fluctuates when the piston connects to the discharge kidney port, as multiple pistons (4 or 5) are connected to the port simultaneously. A slight pressure drop occurs when a piston leaves the port, which is recovered soon after. The number of fluctuations corresponds to the number of pistons connected to the port ahead of the specified piston.

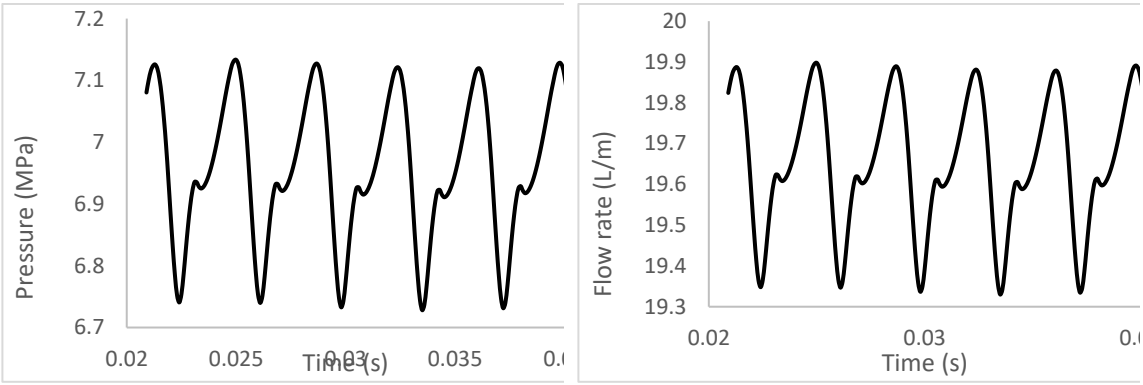

(a) **(b)**

Fig. 17 outlet ripples under 7 MPa and 1440 RPM, (a) pressure ripple, (b) flowrate ripple.

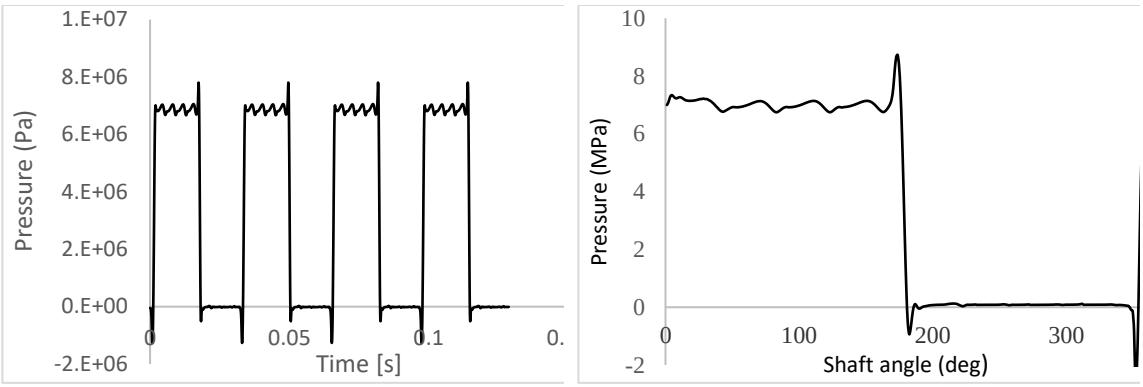

(a) **(b)**

Fig. 18 Piston No. 1 cavity pressure variation over a complete cycle, (a) multicycles, (b) single cycle.

Barrel-Valve Plate Lubrication Pressure

The pressure distribution within the lubrication layer between the barrel and valve plate is depicted in Fig. 19. Which is a combination from hydrostatic and hydrodynamic mechanisms.

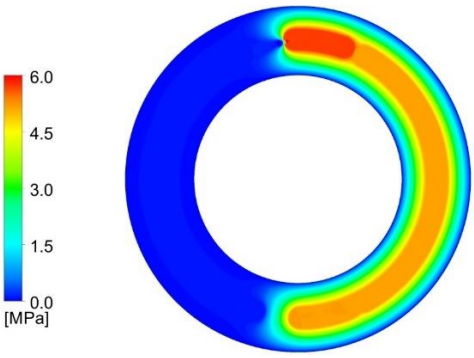

Fig. 19 The pressure distribution over the valve plate surface,7MPa, and 1440 RPM.

Barrel Lubrication Forces

The pressure force trajectory that influences the barrel's position relative to the valve plate is illustrated in Fig. 20. F_v represents the force due to lubrication, which pushes the barrel away from the valve plate, while F_p is the opposing force generated by the internal pressure. These forces are not colinear, resulting in the generation of moments that depend on both pressure and rotational speed. The top pressure force trajectory of the barrel is compared with a similar model by Wang et al., [28], as shown in Fig. 21. The force application point, or pressure center on the discharge side, is nearly aligned with the centerline in both models. The trajectory shape is also similar and varies depending on the pressure level.

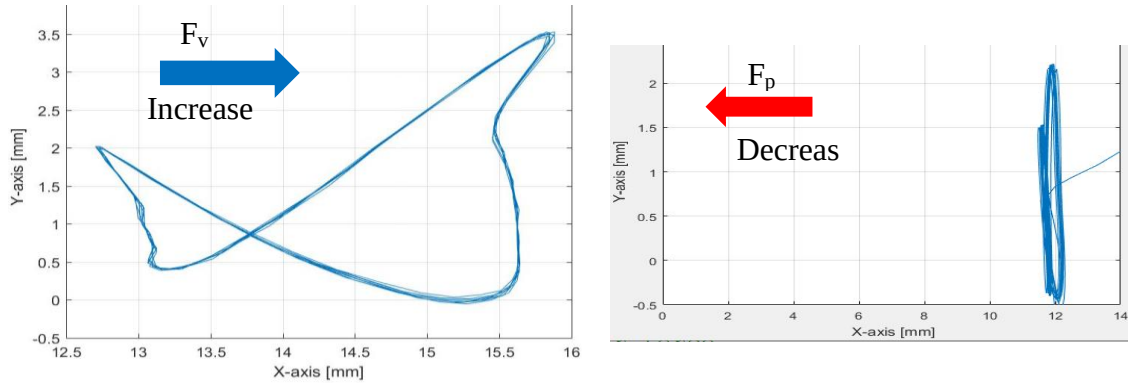

(a) **(b)**

Fig. 20 The pressure force trajectory exerted on the barrel for 15 Mpa,1440 RPM, (a) top surface, (b) inner surface.

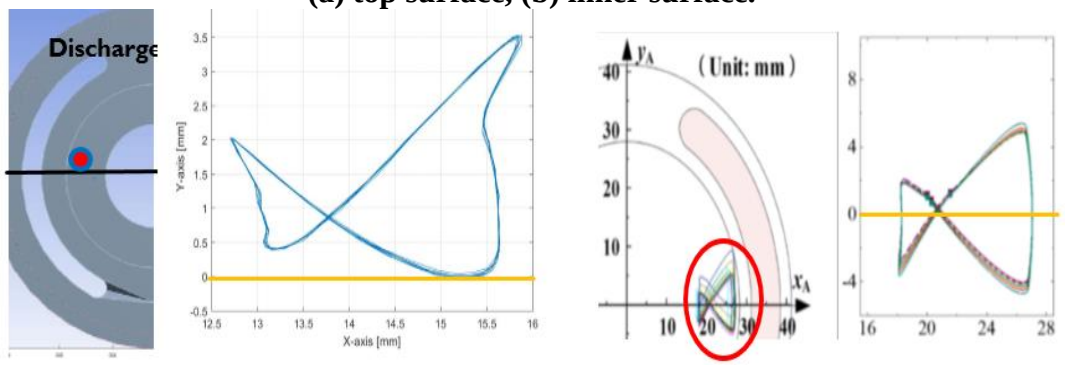

(a) **(b)**

Fig. 21 Barrel top surface pressure force trajectory, (a) present model, (b) Wang's model, [28].

Barrel Tilting Effects on Lubrication Pressure

When the barrel tilts, a wedge-shaped lubrication layer is formed, as shown in Fig. 22. It is depicted that the generated hydrodynamic pressure depends on the tilting angle. As illustrated, the pressure on the suction side is altered due to tilting.

Barrel Tilting Effects on Leakage

As shown in Fig. 23 Barrel tilting increases valve plate leakage, which reduces the pump's volumetric efficiency and may negatively impact its overall performance.

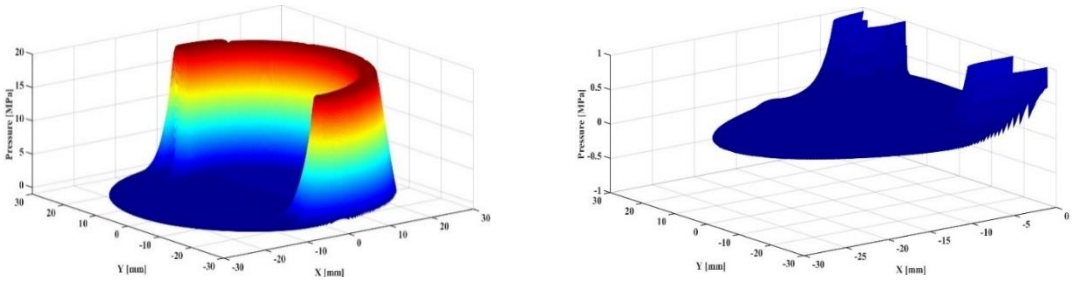

(a) **(b)**

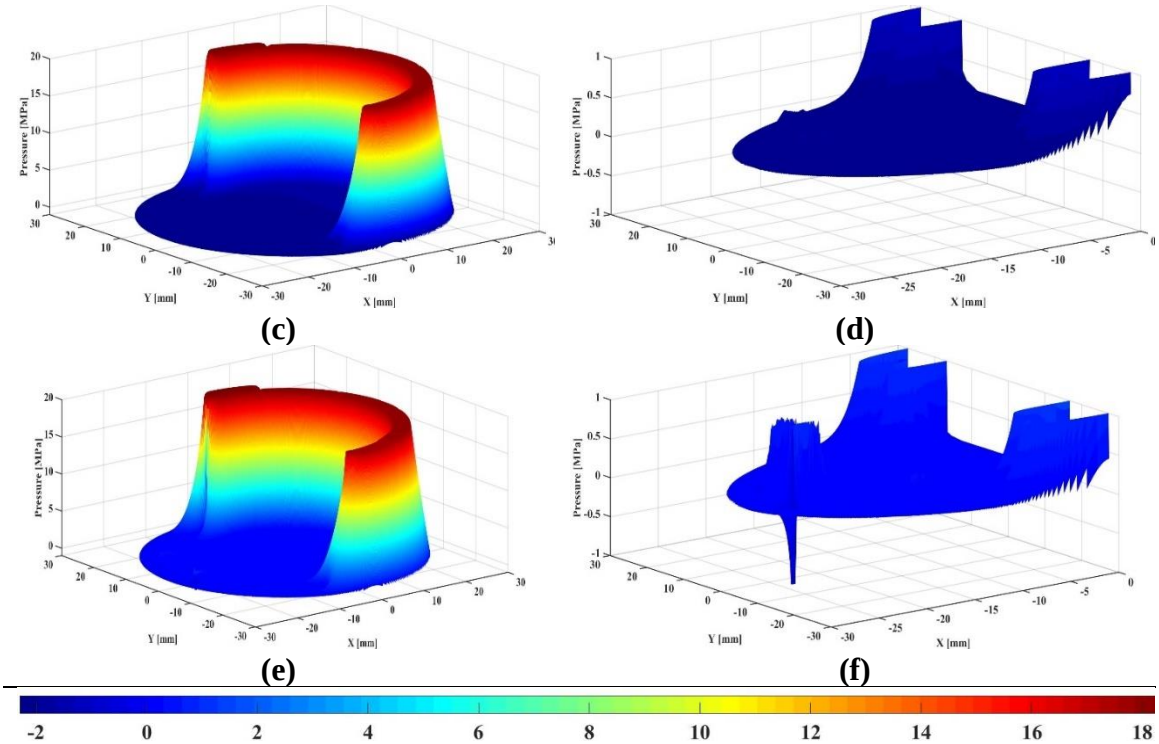

Fig. 22 Barrel-valve plate gap pressure distribution for different tilting angles (a) 0 deg, (c) 0.01 deg, (e) 0.015 deg,(b),(d), and (f) are zooming for suction.

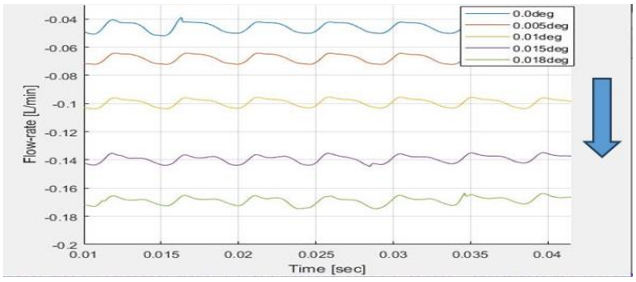

Fig. 23 Valve plate leakage for different barrel tilting angle.

Dynamic model

Valve plate wear height

The valve plate wear height distribution under various operating conditions is illustrated in Fig. 24 - 27. The wear value and its location are dependent on both the discharge pressure and rotational speed.

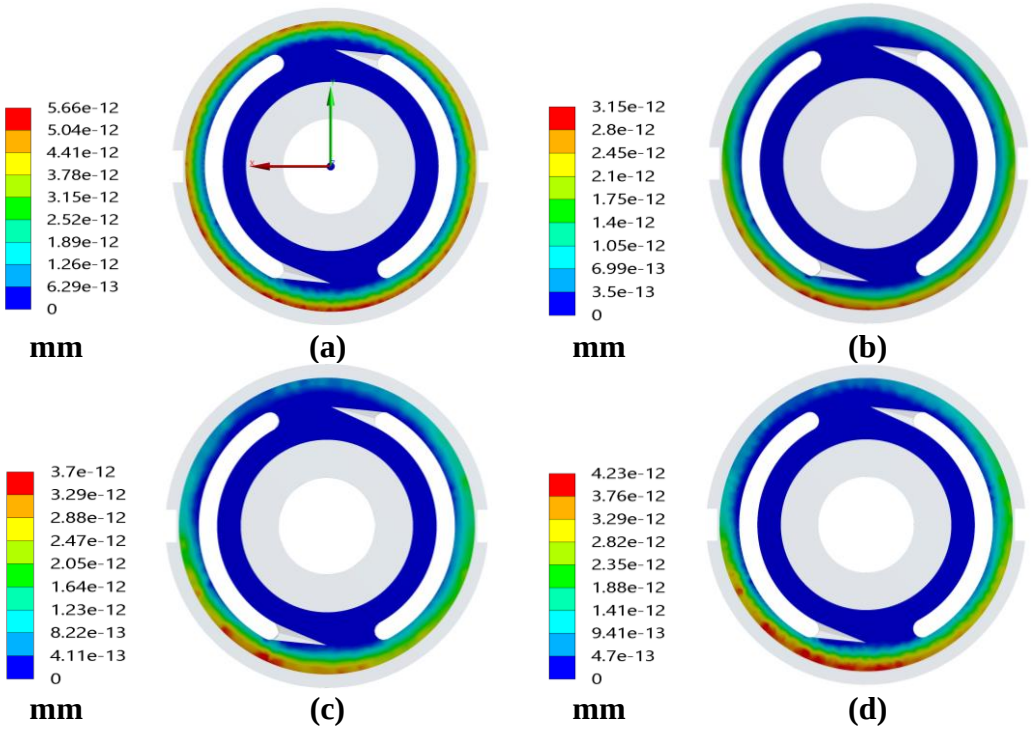

Fig. 24 Wear height at 800 RPM one shaft revolution, (a) 5 MPa, (b) 10 MPa, (c) 15 MPa, and (d) 20 MP.

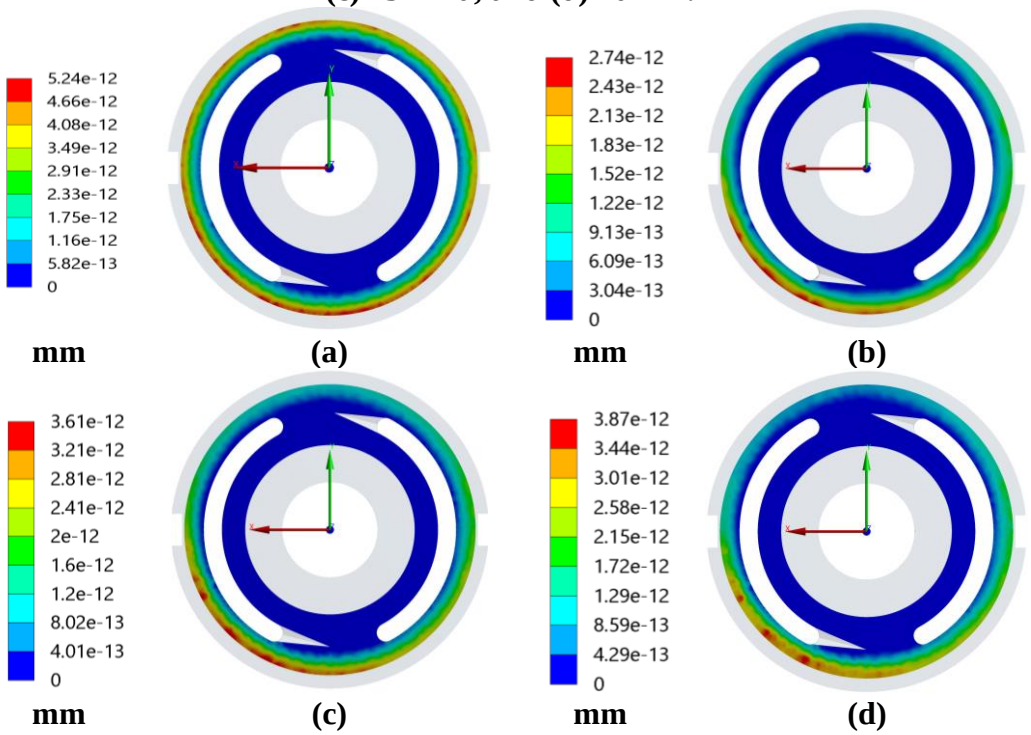

Fig. 25 Wear height at 1200 RPM one shaft revolution, (a) 5 MPa, (b) 10 MPa, (c) 15 MPa, and (d) 20 MPa.

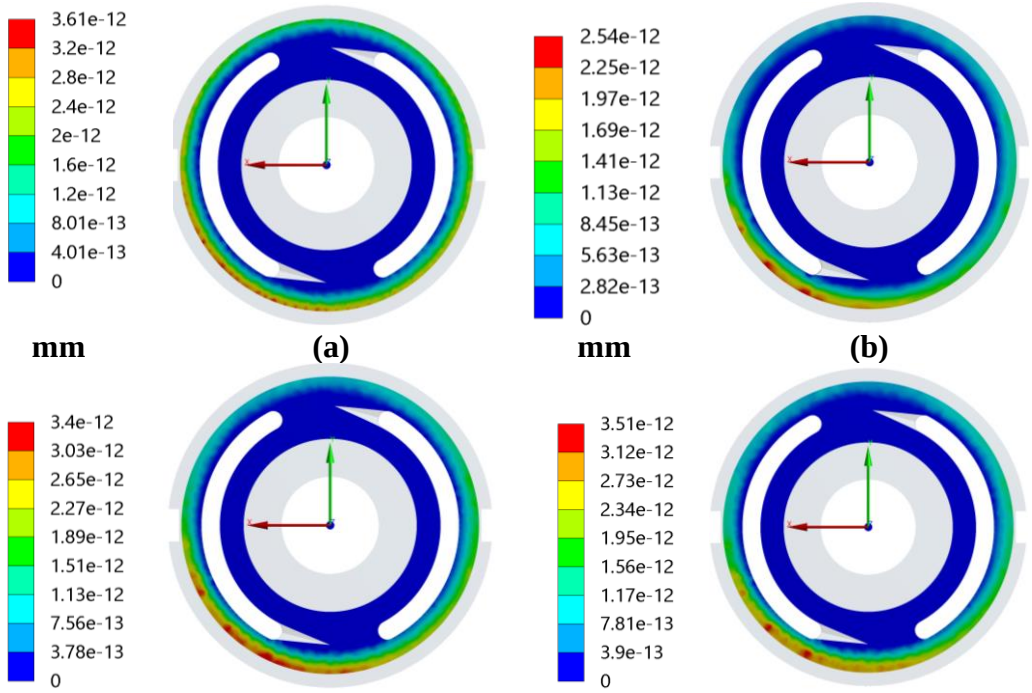

Fig 26 Wear height at 1500 RPM one shaft revolution, (a) 5 MPa, (b) 10 MPa, (c) 15 MPa, and (d) 20 MPa

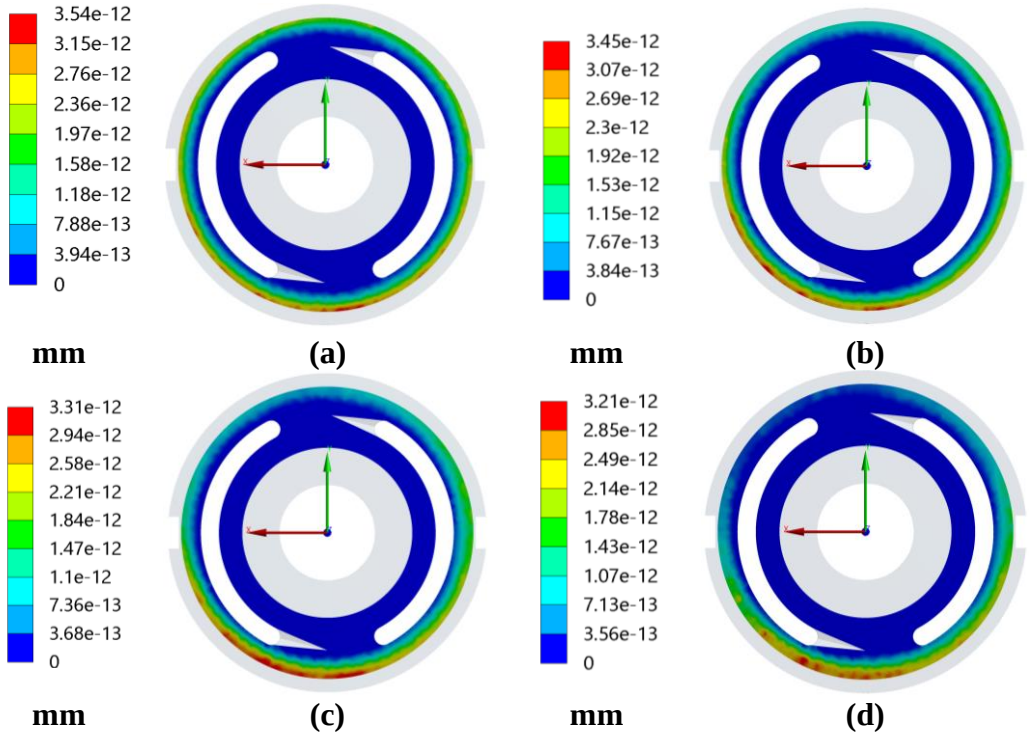

Fig. 27 Wear height at 1800 RPM one shaft revolution, (a) 5 MPa, (b) 10 MPa, (c) 15 MPa, and (d) 20 MPa.

Fig. 28 shows the positive direction used to evaluate wear height variation across the outer radii of the valve plate. As illustrated in Fig. 29, the maximum wear height

occurs within 30 degrees after Top Dead Center (TDC). At low speeds, the maximum wear is located at TDC, but as rotational speed increases, it shifts toward the discharge side. Discharge pressure has minimal influence on the wear location compared to the rotational speed. The wear height distribution of the present model is compared with Jiang et al., [29], in Fig. 30. Both models show higher wear on the discharge side, where the barrel contacts the valve plate, and lower wear on the suction side, where the barrel touches the valve plate more lightly. However, discrepancies in the locations of the maximum and minimum wear points, as well as their values, are observed. These differences are likely due to the present model not accounting for all wear types.

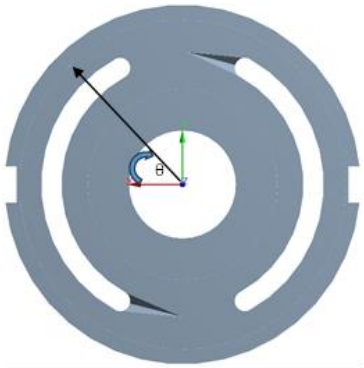

Fig. 28 Measuring the direction of wear height over the valve plate.

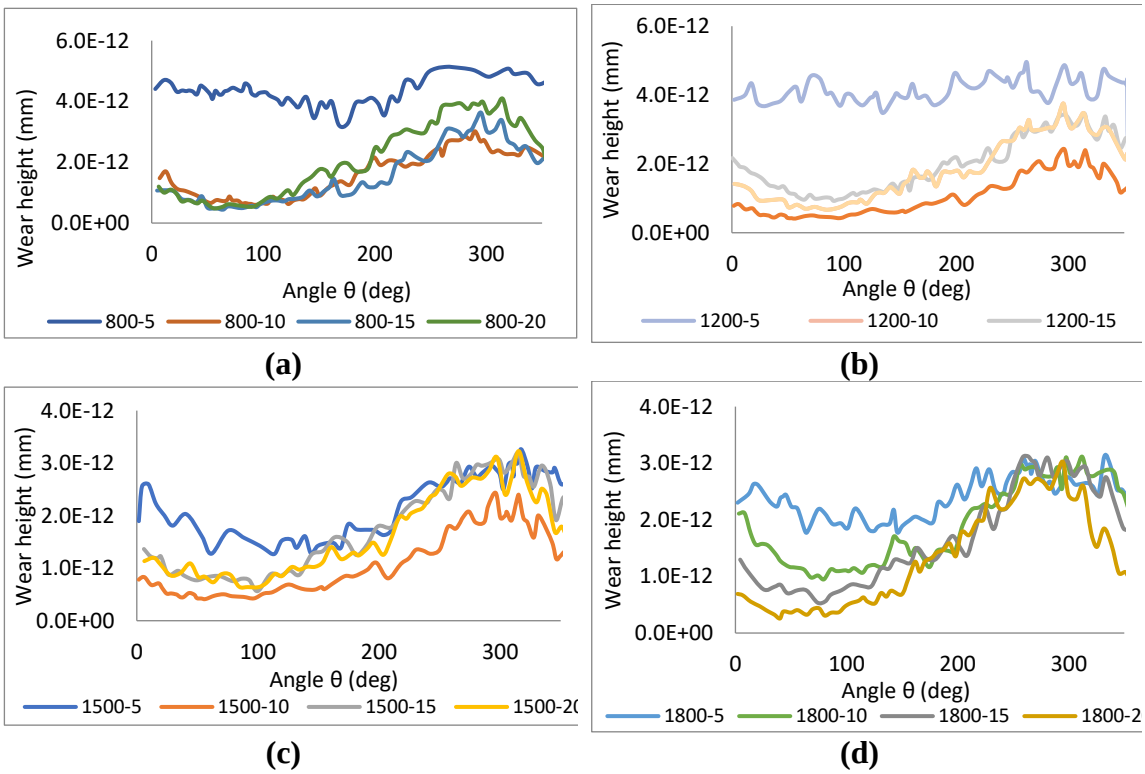

Fig. 29 Wear height distribution over the valve plate for different operating conditions: (a) 800 RPM, (b) 1200 RPM, (c) 1500 RPM, (d) 1800 RPM.

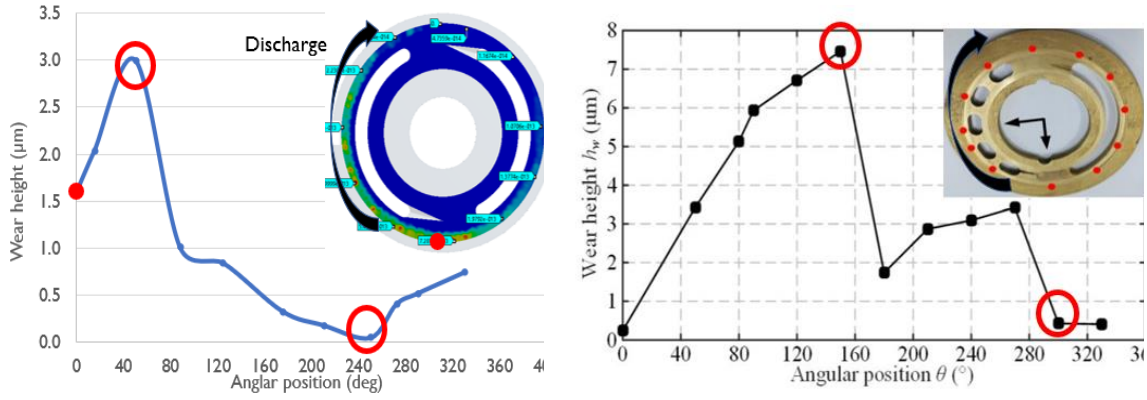

(a) **(b)**

Fig. 30 Wear height distribution over the valve plate, barrel side, (a) current model, (b) experimental finding by Jiang et al., [29].

The wear height at the startup of the first shaft revolution is shown in Fig. 31, illustrating the relationship between wear height and operating conditions. As depicted, at low speeds, the wear rate increases with lower pressure, whereas at higher speeds, the wear rate increases with discharge pressure.

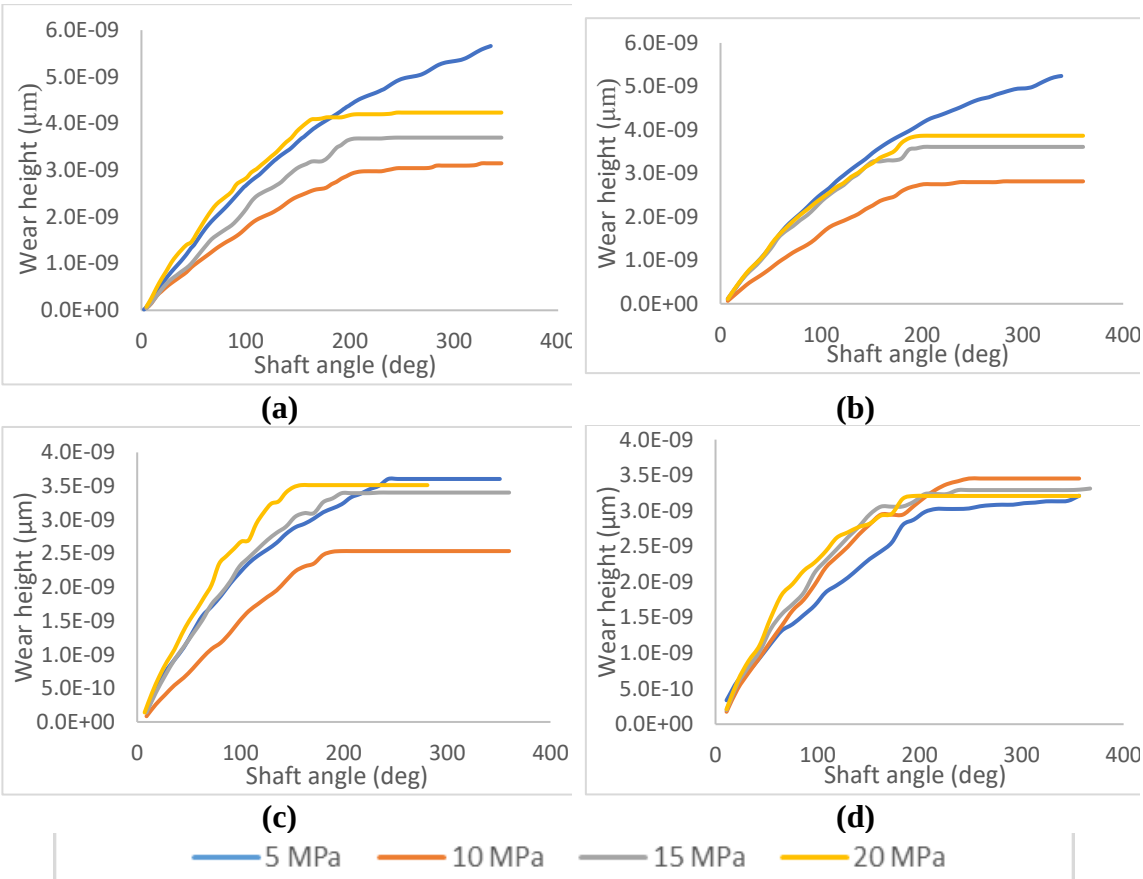

(a) **(b)**

(c) **(d)**

Fig. 31 First shaft revolution of wear height, (a) 800 RPM, (b) 1200 RPM, (c) 1500 RPM, (d) 1800 RPM.

Load Transition Effects

The effect of load transitions, discharge pressure, and/or speed changes is shown in Fig. 32. As observed, wear initiates or reinitiates when the load changes, while during constant operation, the wear rate diminishes.

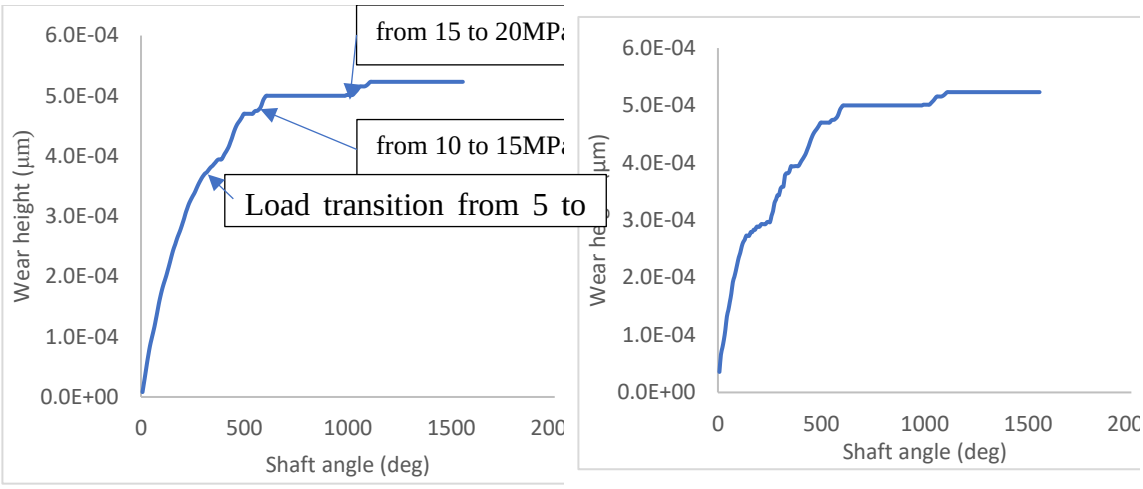

(a) **(b)**

Fig. 32 load transition effect, (a) 800 RPM, (b) 1800 RPM.

Frictional Analysis

The contact pressure between the barrel and valve plate at various rotational speeds is shown in Fig. 33-a. It is illustrated relative to the discharge (resistance) pressure. Similarly, Fig. 33-b shows the frictional torque between the barrel and valve plate, caused by both solid and viscous contacts. Both contact pressure and frictional torque are dependent on rotational speed. Regarding mechanical losses, the barrel's frictional torque varies nonlinearly with operating conditions. At higher speeds, the lubrication-carrying capacity increases, reducing frictional losses and diminishing the effect of pressure. At lower pressures, the reduced oil film carrying capacity leads to higher frictional torque due to increased metal contact. These findings are consistent with those of René Portillo in his thesis, [30], and Miller et al., [31]. Frictional torque increases with high discharge pressure at low and medium rotational speeds, similar to the results of Zhaoqiang Wang et al., [32], who conducted an analytical study on oil film load capacity in axial piston pumps. Their work found that, in addition to load-carrying capacity, the tilting moment increases with discharge pressure, ultimately contributing to valve plate wear.

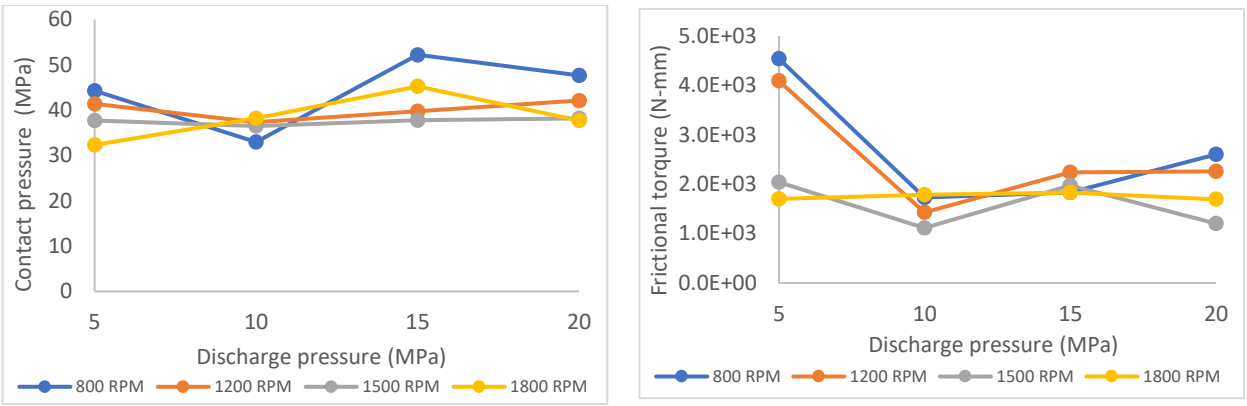

(a) **(b)**

Fig. 33 Tribological parameters of the barrel-valve plate pair for different operating conditions, (a) Contact pressure, (b) Frictional torque.

ANOVA Analysis

The wear height rate is averaged over one revolution, and its variation against the operating conditions is shown in Fig. 34. The significance of discharge pressure and rotational speed on wear height rate is illustrated by the ANOVA analysis in Table 4, where both discharge pressure and rotational speed are identified as significant factors. Fig 35 demonstrates the interaction between pressure and speed, showing that the influence of rotational speed depends on the pressure level, highlighting the interaction of significant factors. The terms P×V (contact pressure multiplied by sliding speed) are the final two terms in the wear height rate equation. Their variation with discharge pressure is shown in Fig 36, which exhibits a similar relationship to the wear height rate as illustrated in Fig. 37.

As illustrated in Fig 35, the wear rate is influenced by both rotational speed and pressure levels. At 5 MPa, the study's lowest discharge pressure, the wear rate increases significantly for a given rotational speed, consistent with the findings of Y. Zhu et al., [33]. However, Diple's experimental work, [34], demonstrated that valve plate wear increases with discharge pressure. These discrepancies arise because the barrel dynamics depend on design parameters specific to each pump, such as the barrel's wetted surface area and spring stiffness. For instance, Peter Achten et al., [35], highlighted the impact of spring stiffness on barrel tilting, showing that barrel tilting can be mitigated with appropriate spring stiffness design criteria. This suggests that pump design is an optimization problem requiring further research to fully understand how each parameter affects wear.

Junhi Zhang et al., [36], examined how operating conditions influence barrel tilting and the lubrication layer's carrying capacity. Their experimental and numerical studies revealed that barrel tilting increases with rotational speed, while low discharge pressures lead to barrel inclination, which in turn increases wear on both the barrel and valve plate. At the top speed (1800 RPM), the wear rate remains nearly constant and is the highest detected wear rate, (Fig 35). The wear rate increases with rotational speed for a given pressure level, while the lowest wear rate across all operating conditions is found at 10 MPa, indicating minimal barrel tilting. At high

pressure and low speed, barrel tilting increases, consistent with the findings of David Richardson et al, [10].

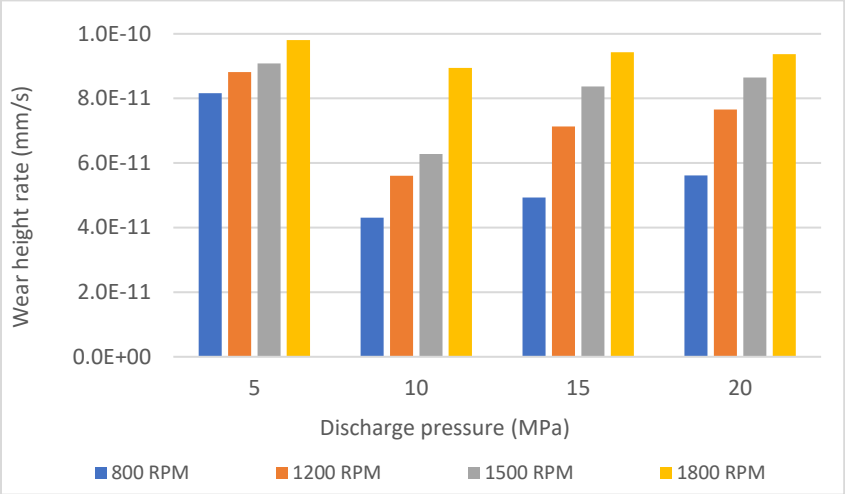

Fig. 34 Wear height rate for different operating conditions

Table 4 ANOVA for main factors.

Source	Sum of Squares	DOF	Mean Square	F-value	p-value	
A-Pressure	1.46E-21	3	4.88E-22	10.27	0.0029	significant
B-Speed	2.77E-21	3	9.23E-22	19.42	0.0003	significant
Residual	4.28E-22	9	4.75E-23			

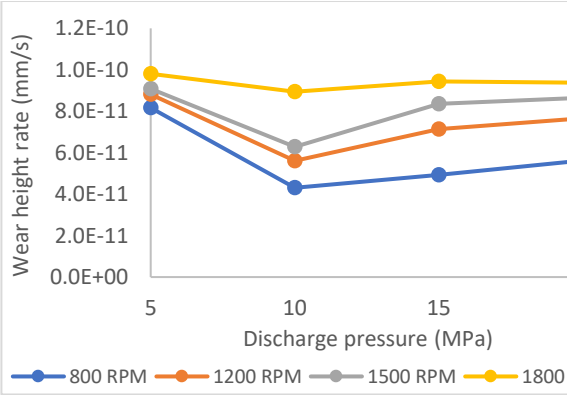

Fig 35. Wear height rate for different pressures and speeds.

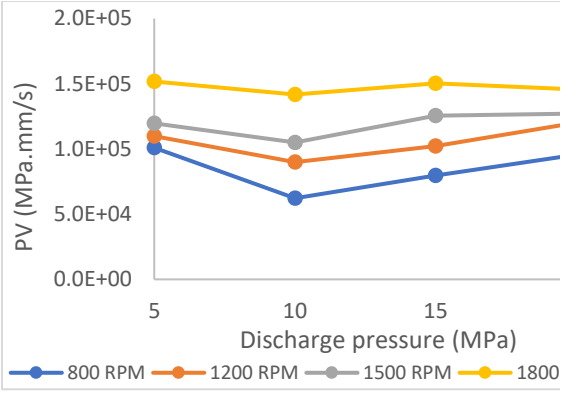

Fig 36. PV variation with operating conditions

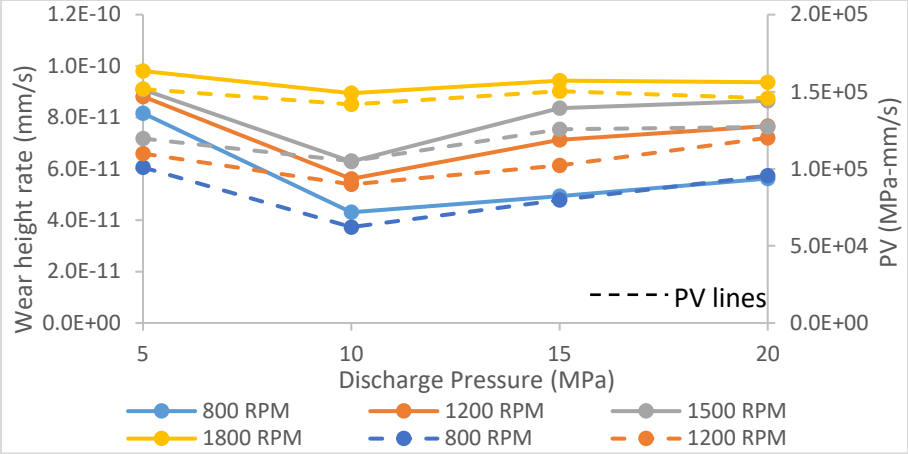

Fig. 37 Wear height rate (solid lines) and PV (dashed lines) explanation with discharge pressure.

Remaining Service Life Estimation

Service life is estimated based on the wear height after 10,000 and 15,000 hours of operation. The pump is considered out of service when the wear height exceeds five times the original gap (i.e., 10μm). The service life under different operating conditions is summarized in Table 5. As noted, the expected service life for such a pump is up to 20,000 hours. From equation (7), the wear rate depends on the wear coefficient k which is selected based on lubrication conditions. Two coefficients have been tested: the first is k=1×10−6, as used in previous calculations, and the second is k=1×10−5. Both cases show similar relationships between operating conditions and wear rates, but with different magnitudes, Fig. 38. Table 5 indicates that the pump's service life is highly dependent on the operating conditions. To extend its service life, the pump should ideally operate near the minimum wear point, which is around 10 MPa, as demonstrated in this study. As shown in Fig. 32, load transitions increase the wear rate, which should be minimized for optimal pump performance.

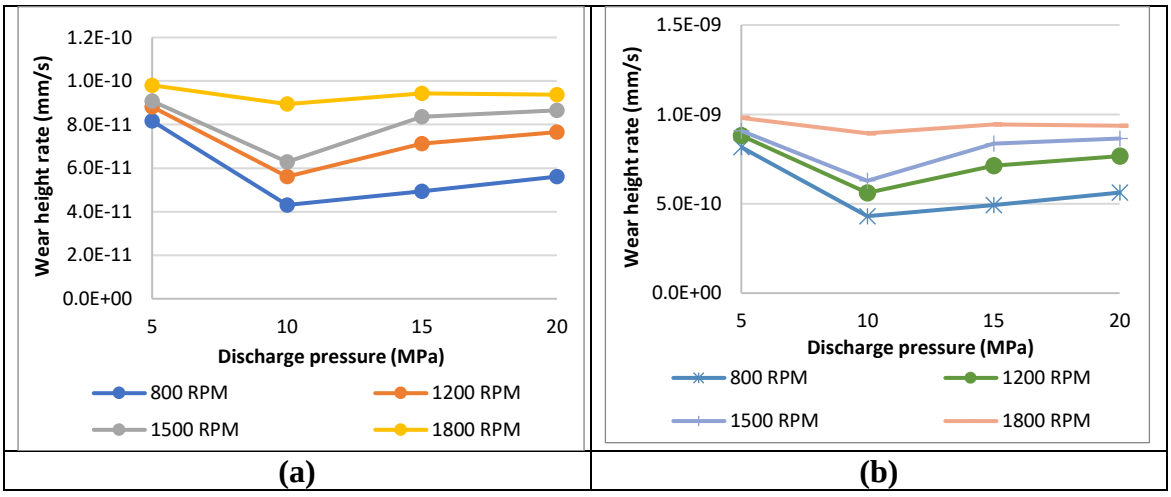

(a) **(b)**

Fig. 38 Wear height rate for different Ks,(a) *k* = 1e-6, (b) *k* = 1e-5.

Table 5 Service life estimation.

		K=1e-6		K=1e-5	
Speed (RPM)	Pressure (MPa)	Service life after 10000 hrs 50% reduction	Service life after 15000 hrs 25% reduction	Service life after 10000 hrs 50% reduction	Service life after 15000 hrs 25% reduction
800	5	Good	Good	Good	Out of service
800	10	Good	Good	Good	Good
800	15	Good	Good	Good	Good
800	20	Good	Good	Good	Good
1200	5	Good	Good	Good	Out of service
1200	10	Good	Good	Good	Good
1200	15	Good	Good	Good	Good
1200	20	Good	Good	Good	Out of service
1500	5	Good	Good	Good	Out of service
1500	10	Good	Good	Good	Good
1500	15	Good	Good	Good	Out of service
1500	20	Good	Good	Good	Out of service
1800	5	Good	Good	Good	Out of service
1800	10	Good	Good	Good	Out of service
1800	15	Good	Good	Good	Out of service
1800	20	Good	Good	Good	Out of service

CONCLUSIONS

Using the finite element methodology (FEM), the wear behavior of an axial piston pump has been numerically investigated. By employing computational fluid dynamics (CFD), the pressure distribution across the barrel's surfaces was estimated and applied as a boundary condition for the Finite Element Model. The model calculates adhesive wear based on Archard's theory to evaluate the barrel's dynamic response. The results indicate that the pump's service life is influenced by both rotational speed and discharge pressure.

The wear rate is minimized at mid-level discharge pressures and speeds, but increases significantly at low discharge pressures and continues to rise with rotational speed at a given pressure. This behavior is primarily due to barrel tilting, driven by the pressure differential between the suction and discharge sides. To extend the pump's service life, reducing load transitions and avoiding low-pressure operation is essential. Additionally, pump design parameters - such as spring stiffness and wetted surface area—should be optimized for better performance and durability. Incorporating real-time fluid-solid interaction techniques could provide more accurate lubrication conditions and improve wear evaluation.

REFERENCES

1. Minav, T.A., et al., Direct pump control effects on the energy efficiency in an electro-hydraulic lifting system. 2011. 4(2): p. 235-242.

2. Esposito, A., *Fluid power with applications*. 2009: Pearson Prentice Hall Columbus, Ohio.
3. Conference, I.F.P., 10th International Fluid Power Conference (10. IFK): March 8-10, 2016 in Dresden. Symposium: Tuesday, March 8. 2016: Dresdner Verein zur Förderung der Fluidtechnik eV Dresden, Institut für ….
4. Mohn, G. and T. Nafz, Swash plate pumps – the key to the future, in 10th International Fluid Power Conference. 2016: Dresden.
5. Guo, S., et al., Hydraulic piston pump in civil aircraft: Current status, future directions and critical technologies. Chinese Journal of Aeronautics, 2020. 33(1): p. 16-30.
6. Ivantysyn, R., A. Shorbagy, and J. Weber. Analysis of the run-in behavior of axial piston pumps. in 2018 Global Fluid Power Society PhD Symposium (GFPS). 2018. IEEE.
7. Sarode, S., L. Shang, and A. Vacca, Numerical Investigation of the Influence of Part Geometric Tolerances on Piston/Cylinder Interface Performance.
8. A.Yamguchi, Formation of A Fluid Film Between A Valve Plate And A Cylinder Block of Piston Pumps And Motors 1st Report. JSME International journal, 1986. 29.
9. A.Yamguchi, Formation of A Fluid Film Between A Valve Plate And A Cylinder Block of Piston Pumps And Motors 2nd Report. JSME International journal, 1986. 30.
10. Richardson, D., et al., Experimental and Analytical Investigation of Floating Valve Plate Motion in an Axial Piston Pump. Tribology Transactions, 2016. 60(3): p. 537-547.
11. Richardson, D., et al., Surface modification effects on lubricant temperature and floating valve plate motion in an axial piston pump. Proceedings of the Institution of Mechanical Engineers, Part J: Journal of Engineering Tribology, 2019. 234(1): p. 3-17.
12. Zhao, J.a., et al., Review of cylinder block/valve plate interface in axial piston pumps: Theoretical models, experimental investigations, and optimal design. Chinese Journal of Aeronautics, 2021. 34(1): p. 111-134.
13. Roselin, F., Simulation of Tribological Contacts in Hydraulic Machines. 2018.
14. Schuhler, G., et al., *Multi technical analysis of wear mechanisms in axial piston pumps.* Journal of Physics: Conference Series, 2017. 843.
15. Zhang, C., et al., Performance Degradation Analysis of Aviation Hydraulic Piston Pump Based on Mixed Wear Theory. Tribology in Industry, 2017. 39(2): p. 248-254.
16. Nilsson, D., *Tribology of hydraulic motor*. 2009, Luleå tekniska university.
17. Li, Z.E., Condition monitoring of axial piston pump. 2005.
18. Andersson, B., et al., *Computational fluid dynamics for engineers*. 2011: Cambridge university press.
19. Ansys®, Theroy Manual, Release 18.1. 2018.
20. Bergada, J.M., et al., *A complete analysis of axial piston pump leakage and output flow ripples.* Applied Mathematical Modelling, 2012. 36(4): p. 1731-1751.
21. Minin, O. and I. Minin, Computational Fluid Dynamics: Technologies and Applications. 2011: BoD–Books on Demand.

22. Ansys® Matreial data base, Release 18.1.
23. Bhushan, B., *Modern tribology handbook*. Vol. 1. 2000: CRC press.
24. Halling, J. and R. Burton, *Principles of tribology*. 1977.
25. Bruce, R.W., Handbook of lubrication and tribology: Theory and design. Vol. 2. 2012: CRC press.
26. Archard, J.J.J.o.a.p., *Contact and rubbing of flat surfaces.* 1953. 24(8): p. 981-988.
27. Apdl solver reference.
28. Wang, T., et al., Modeling and Characteristic Analysis of a Cylinder Block/Valve Plate Interface Oil Film Model for 35 MPa Aviation Piston Pumps. Machines, 2022. 10(12).
29. Jihai, J. and Y. Weipeng, An Approach to Predict Wear Distribution of Valve Plate in Elasto-Hydrodynamic Lubrication. IEEE Access, 2019. 7: p. 86789-86797.
30. 2014_Cylinder Block Valve Plate Interface Performance Investigation Through The Introduction Of Micro Surface Shaping.pdf.
31. Miller, M.K., et al., An Investigation of Hydraulic Motor Efficiency and Tribological Surface Properties. Tribology Transactions, 2014. 57(4): p. 622-630.
32. Wang, Z., et al., *Study on the characteristics of oil film load capacity for axial piston pump.* Australian Journal of Mechanical Engineering, 2018. 18(sup1): p. S140-S150.
33. Zhu, Y., et al., A study on the influence of surface topography on the low-speed tribological performance of port plates in axial piston pumps. Wear, 2015. 338-339: p. 406-417.
34. 2016_Tribolayer Formation on Bronze Cusn12ni2 in the Tribological Contact between Cy linder and Cont rol Plate in an Axial Piston Pump with Swashplate Design.pdf.
35. 2017_Barrel tipping in axial piston pumps and motor.pdf.
36. Zhang, J., et al., Modeling and analysis of the tilt behavior of the cylinder block in a high-speed axial piston pump. 2022. 170: p. 104735.